Quantum programming of the satisfiability problem with Rydberg atom graphs

Seokho Jeong,[1] Minhyuk Kim,[1] Minki Hhan,[2] JuYoung Park,[1] and Jaewook Ahn[1]
[1]*Department of Physics, Korea Advanced Institute of Science and Technology (KAIST), Daejeon 34141, Republic of Korea*
[2]*Quantum Universe Center, Korea Institute for Advanced Science (KIAS), Seoul 02455, Republic of Korea*

(Received 9 January 2023; accepted 26 September 2023; published 12 October 2023)

Finding a quantum computing method to solve nondeterministic polynomial time (NP)-complete problems is currently of paramount importance in quantum information science. Here we propose and experimentally demonstrate a Rydberg atom approach to program the 3-SAT problem, the prototypical NP-complete problem which allows general programming of all NP problems. We use Rydberg atom graphs, each of which consists of Rydberg atom dimers and trimers coupled with quantum wires in the Rydberg blockade interaction regime, to formulate general Boolean expressions, and obtain their many-body ground states to determine the satisfiabilities of the given 3-SAT problem instances quantum mechanically.

DOI: 10.1103/PhysRevResearch.5.043037

I. INTRODUCTION

Currently there are considerable efforts being devoted to making a quantum computer [1–3]. One prominent goal is to engineer a quantum system that can *formulate* quantum algorithms of classically difficult computational problems [4,5]. An efficient algorithm which can solve a problem in the computational complexity class of nondeterministic polynomial (NP)-complete can be used as a subroutine for the efficient algorithm for all other problems in NP, according to the Cook-Levin theorem [6]. So, if a quantum computer can solve an NP-complete problem efficiently, all other NP problems are also efficiently solvable by the polynomial time reduction to the NP-complete problem [7,8].

The Boolean satisfiability problem (SAT or B-SAT) and the 3-SAT problem that has clauses of at most three literals are a prototypical NP-complete problem, i.e., no classical algorithms can efficiently (i.e., in a polynomial time) solve the 3-SAT problem, unless P = NP [9,10]. There are limited physical implementations of the 3-SAT problem, which include an algorithmic conversion to a network-based biocomputation format [11], a quantum circuit approach using Grover's quantum search algorithm in conjunction with the David-Putnam-Logemann-Loveland algorithm [12], and an IBM-Q operation of Grover's quantum algorithm for the 3-SAT problem [13]. These approaches are nonimmune to errors, so it may be worthy to consider the robustness of quantum adiabatic computing.

In this paper, we introduce a quantum algorithm to formulate the 3-SAT problem with Rydberg atoms. Utilizing Rydberg atom dimers and trimers coupled with quantum wires, we formulate a quantum programming algorithm to encode a given 3-SAT problem instance and to evaluate the satisfiability (i.e., the existence of a solution) of the 3-SAT instance experimentally. We utilize the facts that the 3-SAT problem is reducible to the maximum independent set (MIS) problem [14,15], which has been previously implemented with Rydberg atoms [16,17], and that the Rydberg atom MIS approach is reported to be of quantum speedup on computationally hardest graphs over classical simulated annealing [18].

II. THE 3-SATISFIABILITY PROBLEM

The 3-SAT problem is to determine whether a given propositional logic formula (Boolean expression), $\Psi(x_1, x_2, \cdots)$, of Boolean variables, $x_1, x_2, \ldots$, is *satisfiable* (i.e., there exists a set of Boolean values for the variables satisfying the formula) or *unsatisfiable*. The 3-SAT formula $\Psi(x_1, x_2, \cdots)$ is given in the conjunctive normal form [19], i.e., a conjunction of N_C clauses, $\Psi(x_1, x_2, \cdots, x_n) = \bigwedge_{j=1}^{N_C} C_j$, where each clause, $C_j = \ell_{j,1} \vee \ell_{j,2}$ or $\ell_{j,1} \vee \ell_{j,2} \vee \ell_{j,3}$, is a disjunction of at most three literals, $\ell_{j,1}, \ell_{j,2}, \ell_{j,3} \in \{x_k, \bar{x}_k | k = 1, \cdots, n\}$ [20,21].

The given 3-SAT problem can be reduced to the MIS problem for an MIS graph $G(V, E)$, given by

$$V = \left\{(j,k) | \ell_{j,k} \in C_j\right\}, \tag{1a}$$

$$E = E_1 \cup E_2, \tag{1b}$$

$$E_1 = \{[(j,k_1),(j,k_2)] | k_1 \neq k_2\}, \tag{1c}$$

$$E_2 = \{[(j_1,k_1),(j_2,k_2)] | k_1 \neq k_2, \ell_{j_1,k_1} = \bar{\ell}_{j_2,k_2}\}, \tag{1d}$$

where V is the set of vertices of which an element (j, k) corresponds to the literal $\ell_{j,k}$ in the jth clause C_j; E is the set of all edges, the union of two edge sets E_1 and E_2; E_1 is the set of all intraclause edges connecting two vertices in the same clause C_j; and E_2 is the set of all interclause edges which connect two vertices in different clauses, whose corresponding literals are negation to each other [14,15].

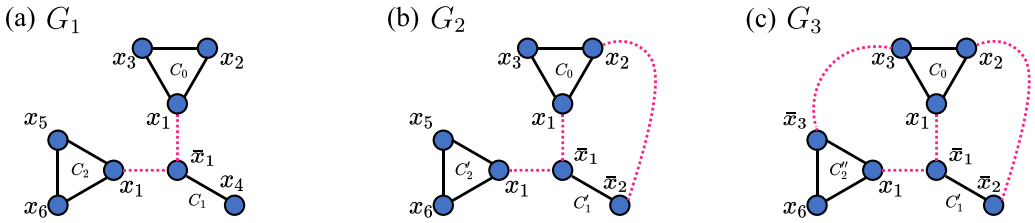

FIG. 1. (a) The MIS graph G_1 reduced from the 3-SAT instance Ψ_1 in Eqs. (2), (b) G_2 from Ψ_2, and (c) G_3 from Ψ_3, where vertices represent literals ($x_1, \cdots, x_6$ and negations), solid edges intraclause logics, and dashed edges the interclause logics (between literals and their negations).

Figure 1 shows examples of MIS graphs obtained with the above reduction algorithm in Eq. (1). The first graph, G_1 in Fig. 1(a), is for a 3-SAT instance, given by

$$\Psi_1(x_1, x_2, x_3, x_4, x_5, x_6) = C_0 \wedge C_1 \wedge C_2, \tag{2a}$$

$$C_0 = x_1 \vee x_2 \vee x_3, \tag{2b}$$

$$C_1 = \bar{x}_1 \vee x_4, \tag{2c}$$

$$C_2 = x_1 \vee x_5 \vee x_6, \tag{2d}$$

where the clauses having two or three literals are respectively mapped to the dimers or trimers (of solid edges) and the literal-negation pairs are mapped to the interclause edges (of dashed lines). Similarly, we define two more MIS graphs G_2 and G_3 for $\Psi_2 = C_0 \wedge C_1' \wedge C_2$ and $\Psi_3 = C_0 \wedge C_1' \wedge C_2'$, with $C_1' = \bar{x}_1 \vee \bar{x}_2$ and $C_2' = x_1 \vee \bar{x}_3 \vee x_6$, as respectively shown in Figs. 1(b) and 1(c).

III. RYDBERG ATOM GRAPHS

Rydberg atoms have been used to solve the MIS problems [16–18,22,23]. The Hamiltonian of Rydberg atoms arranged for an MIS graph G is given (in $\hbar = 1$ units) by

$$\hat{H}(G) = \sum_{(j,k)\in E(G)} U\hat{n}_j\hat{n}_k - \sum_{j\in V(G)} \left(\Delta\hat{n}_j - \frac{\Omega}{2}\hat{\sigma}_x^{(j)}\right), \tag{3}$$

where U is the interaction between edged atoms, Ω and Δ are the Rabi frequency and detuning of Rydberg excitation, and $\hat{n}_j = (1 - \hat{\sigma}_z^{(j)})/2$, $\hat{\sigma}_x^{(j)}$, $\hat{\sigma}_z^{(j)}$ are the excitation and Pauli operators defined for the ground ($|0\rangle$) and Rydberg ($|1\rangle$) states of the jth atom. In the limit of $\Omega \to 0$, many-body ground states of $\hat{H}(G)$ correspond to the MIS solutions of G, because $U > 0$ means the MIS problem's constraint that only one vertex can be in MIS for any two vertices on the same edge, satisfying the condition of the independent set, and $0 < \Delta < U$ maximizes the number of vertices in the independent set.

The MIS graphs in Fig. 1 are physically implementable with experimental graphs, $G_1^{\rm Exp}$, $G_2^{\rm Exp}$, and $G_3^{\rm Exp}$, in Figs. 2(a)–2(c), where the "normal" edges (solid line edges) are between Rydberg blockaded pairs of atoms and long-distance edges (dashed, interclause edges) are implemented with Rydberg quantum wires [17,23,24]. In Fig. 2(a) for Ψ_1, x_1 in C_0 and C_2 are edged to $\bar{x}_1$ in C_1, by placing the atom trios, C_0 (upper)–C_1 (lower right) and C_1 (lower right)–C_2 (lower left) closely, so that the atoms x_1 in C_0 (respectively, also in C_2) and $\bar{x}_1$ are at the distance d. In Fig. 2(b), the long edge between x_2 and $\bar{x}_2$ of $G_2^{\rm Exp}$ is implemented with a Rydberg quantum wire of two auxiliary atoms labeled by $\{a_1, a_2\}$. Also, in Fig. 2(c), the two long edges x_2-$\bar{x}_2$ and x_3-$\bar{x}_3$ of $G_3^{\rm Exp}$ are implemented respectively with two Rydberg quantum wires respectively with auxiliary atoms, $\{a_1, a_2\}$ and $\{a_3, a_4\}$, respectively. These wire atoms mediate the Rydberg blockade between two literal atoms with far distance [17,24,25]. The many-body ground states of $\hat{H}(G)$ for $G = G_1^{\rm Exp}$, $G_2^{\rm Exp}$, and $G_3^{\rm Exp}$ are summarized in Table I.

The positions of all atoms (literals and auxiliary atoms) of $G_3^{\rm Exp}$ are obtained under the conditions that the distances of all edged atoms (including auxiliary atoms) are kept nearly at the same interatom distance, $d = 7.0$ μm, smaller than the Rydberg blockade distance $d_B = 10.0$ μm, and that all un-edged atoms are separated more than $\sqrt{2}d$. For this, we minimized the overlap integral defined by

$$F = \pi \sum_{(i,j)\in E} \int_{\frac{|\vec{r}_{ij}|}{2}}^{\frac{d}{2}} \left(\frac{d^2}{4} - r^2\right) dr + \frac{\pi}{\sqrt{8}} \sum_{(i,j)\notin E} \int_{\frac{|\vec{r}_{ij}|}{2}}^{\frac{d}{\sqrt{2}}} \left(\frac{d^2}{2} - r^2\right) dr\Theta(\sqrt{2}d - |\vec{r}_{ij}|), \tag{4}$$

where $\vec{r}_{ij}$ is the displacement vector from the ith atom to the jth atom, and $\Theta(x)$ is the Heaviside step function (1 for $x > 0$, 0 for $x < 0$). The first term in Eq. (4) is the overlap of the unit spheres of all edged atoms, which is minimized for the spheres to be as close as possible. The second term is the overlap of the $\sqrt{2}d$-size spheres of all un-edged atoms, where the Heaviside function ensures the distance between un-edged atoms to be more than $\sqrt{2}d$. $G_1^{\rm Exp}$ and $G_2^{\rm Exp}$ are then obtained as graph minors of $G_3^{\rm Exp}$. The positions of the atoms of these graphs are listed in Table II, along with $G_1^{\rm Alt}$, to be discussed in Sec. VI.

IV. RYDBERG ATOM EXPERIMENT

To solve the 3-SAT problem quantum mechanically, we perform many-body ground-state searching experiments with Rydberg atoms arranged for the corresponding MIS graphs. The experimental setup is a Rydberg atom quantum annealing machine, which consists of a cold atom apparatus, an optical tweezer array system, a Rydberg excitation laser system, and a detection apparatus [17,22,23,26]. The cold atom apparatus is a magneto-optical trap (MOT), in which atoms (rubidium, ^{87}Rb) are cooled in a vacuum chamber (2.6×10^{-10} Torr) down to a temperature around 25 μK by Doppler and polarization gradient cooling and optically pumped to the ground hyperfine state $|0\rangle = |5S_{1/2}, F = 2, m_F = 2\rangle$. The optical tweezer array system uses a spatial light modulator

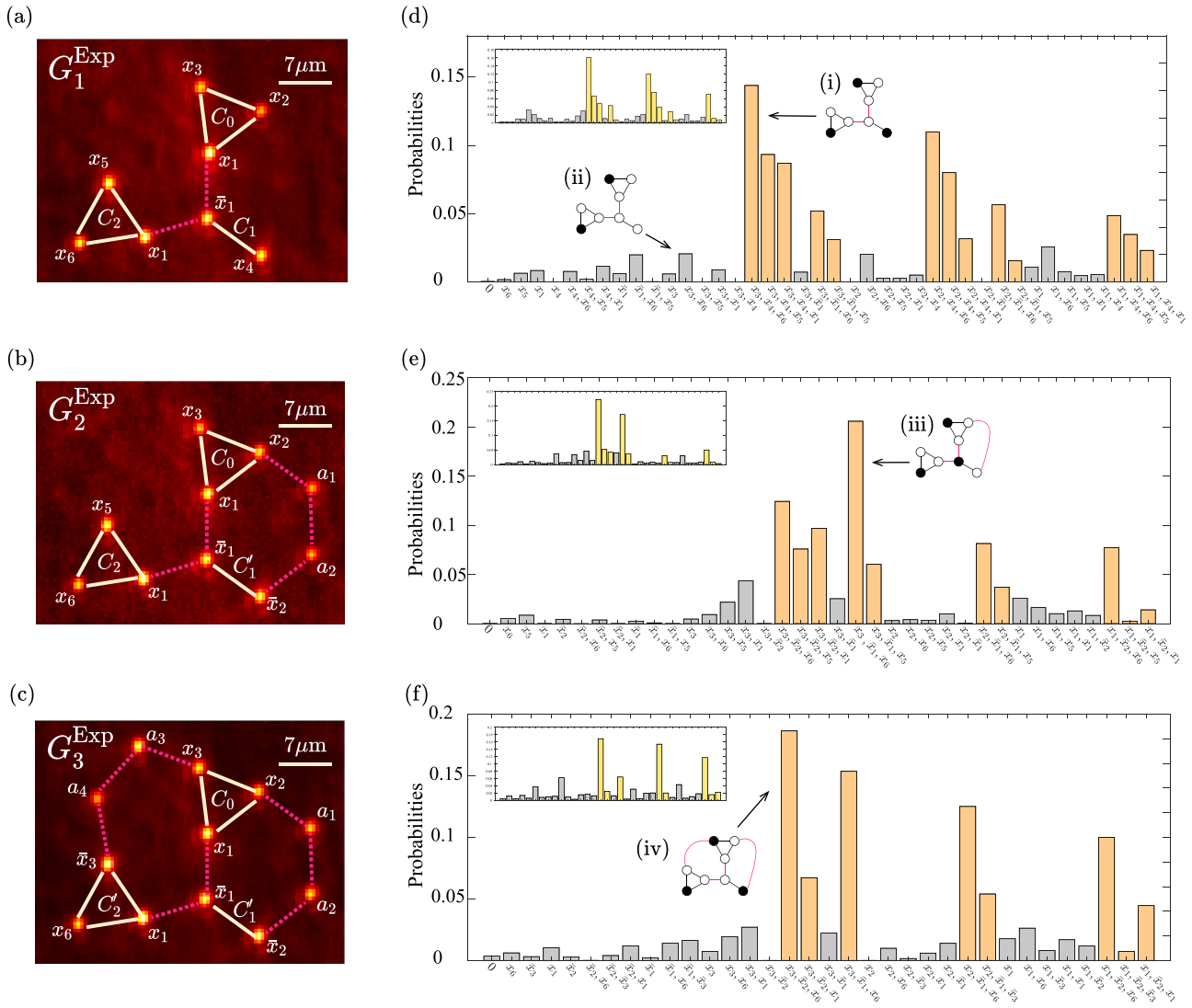

FIG. 2. (a) Experimental MIS graph G_1^{Exp}, (b) G_2^{Exp}, and (c) G_3^{Exp} of literal atoms $(x_1, \cdots, x_6)$ and quantum wire atoms $(a_1, \cdots, a_4)$. (d) Maximum likelihood probabilities of G_1^{Exp} experiments, where the x axis denotes literal atoms in $|1\rangle$ in each binary configuration. (e) G_2^{Exp} experiments. (f) G_3^{Exp} experiments. For example, the peak (i) corresponds to $|x_1x_2x_3; x_4; x_5x_6\rangle = |001; 1; 001\rangle$, (ii) $|001; 0; 001\rangle$, (iii) $|x_1x_2x_3; x_5x_6\rangle = |001; 01\rangle$, and (iv) $|x_1x_2x_3; x_6\rangle = |001; 1\rangle$. Insets in (d)–(f) show numerical simulations with $\gamma = 30\ (2\pi)$ kHz of laser phase and dephasing noise taken into account.

(Meadowlarks ODPDM512) and an off-resonant 820-nm laser (a Ti:sapphire CW laser from Avesta) to produce a three-dimensional array of optical tweezers which capture single atoms and arrange them at target positions. The distance of all edged atoms is $d = 7.0$ μm, which is smaller than Rydberg blockade distance $r_B = 10$ μm. The van der Waals interaction of the edged atoms at is $U/(2\pi) = 8.70$ MHz. The Rydberg excitation laser system excites the ground-state atoms to the Rydberg state $|1\rangle = |71S_{1/2}, m_J = 1/2\rangle$ by the two-photon process through the near-resonant intermediate state $|i\rangle = |5P_{3/2}, F' = 3, m'_F = 3\rangle$, utilizing 780-nm (a homemade external-cavity diode laser) and 480-nm (Toptica TA-SHG Pro) lasers, of which the laser frequencies are stabilized down to a narrow linewidth of $<30\ (2\pi)$ kHz with a proportional-integral-derivative (PID) controller (Toptica FALC 110) and an ultralow expansion (ULE) cavity (Stable Laser Systems, finesse 15 000). The two-photon Rabi frequency at the intensity peak of the lasers is $\Omega_0 = \Omega_{0i}\Omega_{i1}/2\Delta_m = 1\ (2\pi)$ MHz, where $\Omega_{0i} = 93\ (2\pi)$ MHz and $\Omega_{i1} = 14\ (2\pi)$ MHz are the one-photon Rabi frequencies for the $|0\rangle$-$|i\rangle$ and $|i\rangle$-$|1\rangle$ transitions, respectively, and $\Delta_m = 660\ (2\pi)$ MHz is the intermediate detuning. The detection apparatus combines an electron-multiplying charge-coupled device (Andor iXon Ultra 897) and an electrically tunable lens (ETL, EL-16-40-TC of Optotune) to image the fluorescence of ground-state single atoms via the $|5S_{1/2}, F = 2\rangle$-$|5P_{3/2}, F = 3\rangle$ transition.

The experimental procedure of the quantum computing of the 3-SAT problem starts with an experimental MIS graph, chosen among $G_{1,2,3}^{\text{Exp}}$, of atoms arranged with optical tweezers and initially prepared in $|0\rangle^{\otimes|G|}$. After we turn off all the optical tweezers, we turn on Rydberg excitation and adiabatically

TABLE I. Many-body ground states of G_1^{Exp}, G_2^{Exp}, and G_3^{Exp} graphs represented in symmetric base states defined by $|S_1\rangle = (|001;01;100\rangle + |010;01;100\rangle)/\sqrt{2}$, $|S_2\rangle = (|001;01;001\rangle + |001;01;010\rangle)/\sqrt{2}$, $|S_3\rangle = (|001;10;001\rangle + |001;10;010\rangle)/\sqrt{2}$, $|S_4\rangle = (|010;01;001\rangle + |010;01;010\rangle)/\sqrt{2}$, $|S_5\rangle = (|010;10;001\rangle + |010;10;010\rangle)/\sqrt{2}$, and $|S_6\rangle = (|100;01;001\rangle + |100;01;010\rangle)/\sqrt{2}$.

Graph	State representation	Many-body ground states of $\hat{H}(G_{1,2,3}^{\mathrm{Exp}})$ in their MIS phase
G_1^{Exp}	$\lvert x_1x_2x_3;\bar{x}_1x_4;x_1x_5x_6\rangle$	$\sqrt{\frac{49}{200}}(\lvert S_2\rangle + \lvert S_4\rangle) + \sqrt{\frac{9}{50}}(\lvert S_1\rangle + \lvert S_6\rangle)$ $+\sqrt{\frac{3}{50}}\lvert 100;01;100\rangle + \sqrt{\frac{9}{200}}(\lvert S_3\rangle + \lvert S_5\rangle)$
G_2^{Exp}	$\lvert x_1x_2x_3;\bar{x}_1\bar{x}_2;x_1x_5x_6\rangle \otimes \lvert a_1a_2\rangle$	$\sqrt{\frac{1}{50}}\lvert S_3\rangle \otimes (\sqrt{\frac{18}{10}}\lvert 01\rangle + \sqrt{\frac{63}{10}}\lvert 10\rangle) + \sqrt{\frac{3}{500}}\lvert S_5\rangle \otimes \lvert 01\rangle$ $+(\sqrt{\frac{197}{500}}\lvert S_2\rangle + \sqrt{\frac{107}{500}}\lvert S_6\rangle) \otimes \lvert 10\rangle$ $+(\sqrt{\frac{131}{1000}}\lvert 001;01;100\rangle + \sqrt{\frac{93}{1000}}\lvert 100;01;100\rangle) \otimes \lvert 10\rangle$
G_3^{Exp}	$\lvert x_1x_2x_3;\bar{x}_1\bar{x}_2;x_1\bar{x}_3x_6\rangle \otimes \lvert a_1a_2\rangle \otimes \lvert a_3a_4\rangle$	$\sqrt{\frac{1}{1000}}\lvert 001;10;001\rangle \otimes (\sqrt{46}\lvert 01\rangle + \sqrt{53}\lvert 10\rangle) \otimes \lvert 01\rangle$ $+\sqrt{\frac{46}{1000}}\lvert 010;10;001\rangle \otimes \lvert 01\rangle \otimes (\lvert 01\rangle + \lvert 10\rangle)$ $+\sqrt{\frac{17}{1000}}\lvert 010;10;010\rangle \otimes \lvert 01\rangle \otimes \lvert 10\rangle$ $+(\sqrt{\frac{121}{1000}}\lvert 001;01;001\rangle + \sqrt{\frac{65}{1000}}\lvert 001;01;100\rangle) \otimes \lvert 10\rangle \otimes \lvert 01\rangle$ $+\sqrt{\frac{46}{1000}}\lvert 100;01;010\rangle \otimes \lvert 10\rangle \otimes \lvert 10\rangle$ $+(\sqrt{\frac{4}{25}}\lvert 100;01;001\rangle + \sqrt{\frac{3}{25}}\lvert 100;01;100\rangle) \otimes \lvert 10\rangle \otimes (\lvert 01\rangle + \lvert 10\rangle)$

change the Hamiltonian from $\hat{H}(\Delta = -0.7\Delta_0, \Omega = 0, t = 0)$ for the paramagnetic phase to $\hat{H}(\Delta = \Delta_0, \Omega = 0, t = t_f)$ for the MIS phase, along the control path denoted in the phase diagram [27,28] in Fig. 3. The control parameters Ω and Δ are changed with a radio-frequency synthesizer (Moglabs XRF) and acousto-optic modulators (AOMs) in a method similar to that introduced in Refs. [22,23], with $\Omega_0/(2\pi) = 1.0\,\mathrm{MHz}$, $\Delta_0/(2\pi) = 5\,\mathrm{MHz}$, and $t_f = 2.88$ μs. After the quantum annealing, all optical tweezers are turned back to recapture resulting ground-state atoms, which are then imaged to record a resulting experimental MIS solution. The above procedure is repeated $M = 5235$, 5000, and 8000 times for G_1^{Exp}, G_2^{Exp}, and G_3^{Exp} graphs, respectively, to obtain the probability distribution of all $2^{|G|}$ binary-spin configurations of all atoms.

TABLE II. Atom positions of G_1^{Exp}, G_2^{Exp}, G_3^{Exp}, and G_1^{Alt}.

Graphs	Atom positions (x, y, z) (μm)			
G_1^{Exp}	x_1:	$(-1.51, -0.97, 0)$	x_2:	$(4.01, -5.28, 0)$
	x_3:	$(-2.49, -7.90, 0)$	$\bar{x}_1$:	$(-1.70, 6.03, 0)$
	x_4:	$(4.09, 9.97, 0)$	x_1:	$(-8.47, 7.80, 0)$
	x_5:	$(-12.35, 1.97, 0)$	x_6:	$(-15.46, 8.24, 0)$
G_2^{Exp}	x_1:	$(-1.51, -0.97, 0)$	x_2:	$(4.01, -5.28, 0)$
	x_3:	$(-2.49, -7.90, 0)$	$\bar{x}_1$:	$(-1.50, 6.03, 0)$
	$\bar{x}_2$:	$(4.09, 9.97, 0)$	x_1:	$(-8.47, 7.80, 0)$
	x_5:	$(-12.35, 1.97, 0)$	x_6:	$(-15.46, 8.24, 0)$
	a_1:	$(9.69, -1.20, 0)$	a_2:	$(9.71, 5.80, 0)$
G_3^{Exp}	x_1:	$(-1.51, -0.97, 0)$	x_2:	$(4.01, -5.28, 0)$
	x_3:	$(-2.49, -7.90, 0)$	$\bar{x}_1$:	$(-1.50, 6.03, 0)$
	$\bar{x}_2$:	$(4.09, 9.97, 0)$	x_1:	$(-8.47, 7.80, 0)$
	$\bar{x}_3$:	$(-12.35, 1.97, 0)$	x_6:	$(-15.46, 8.24, 0)$
	a_1:	$(9.69, -1.20, 0)$	a_2:	$(9.71, 5.80, 0)$
	a_3:	$(-9.05, -10.36, 0)$	a_4:	$(-13.50, -4.93, 0)$
G_1^{Alt}	x_1:	$(-7.20, 0.03, 0)$	x_2:	$(-13.44, 3.60, 0)$
	x_3:	$(-13.44, -3.60, 0)$	$\bar{x}_1$:	$(0, 0, 0)$
	x_4:	$(3.60, 0, 6.24)$	x_1:	$(3.60, 0, -6.24)$
	x_5:	$(3.60, 0, -13.44)$	x_6:	$(9.84, 0, -9.84)$

V. RESULTS AND ANALYSIS

Experimental results are shown in Figs. 2(d)–2(f) for G_1^{Exp}, G_2^{Exp}, and G_3^{Exp}, respectively, where the experimentally most likely probabilities are plotted for all binary configurations of literal atoms with the x axis denoting atoms in $|1\rangle$ only, and all antiblockade atom configurations (of little probabili-

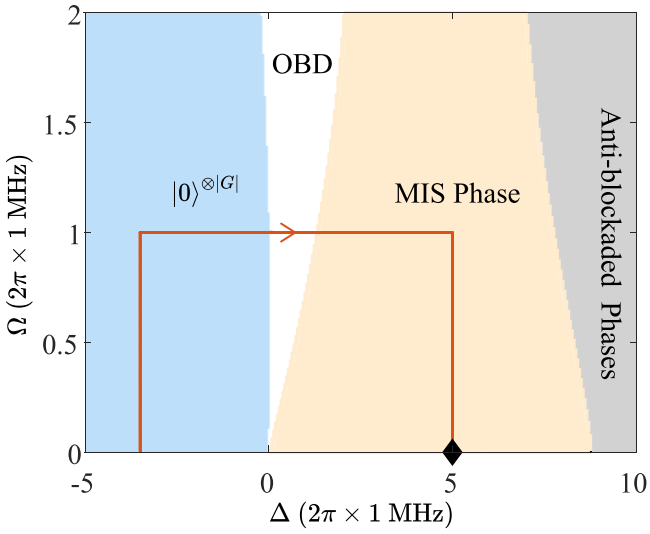

FIG. 3. Phase diagram of $\hat{H}(G_1^{\mathrm{Exp}})$ with the control path is shown with an arrow from the paramagnetic phase via the order-by-disorder (OBD) phase to the MIS phase. The phase diagrams of $\hat{H}(G_2^{\mathrm{Exp}})$ and $\hat{H}(G_3^{\mathrm{Exp}})$ are similar.

ties) are omitted for the sake of presentation. The maximum likelihood probability calculation [29] assumed state preparation and measurement (SPAM) errors [30], $P(1 \mid 0) = 3.9\%$ and $P(0 \mid 1) = 7.9\%$, which are experimentally calibrated. Also the Rydberg quantum-wire compilation method [23] is used to impose the antiferromagnetic atom chain condition, $|a_1 a_2\rangle$ and $|a_3 a_4\rangle = |01\rangle$ or $|10\rangle$ among collected experimental data. In Figs. 2(d)–2(f), orange bars are the 3-SAT solution states with one atom excited in each clause, while gray bars are nonsolution states. For example, in Fig. 2(d) for G_1^{Exp}, the maximal peak (i) of $|x_1, x_2, x_3; \bar{x}_1 x_4; x_1, x_5, x_6\rangle = |001; 01; 001\rangle$ is a 3-SAT solution and the peak (ii) of $|001; 00; 001\rangle$, in which two atoms in C_1 and C_0 are excited but none in C_1, is not a solution. Similarly, most of the dominant peaks in Figs. 2(d)–2(f) are verified to be 3-SAT solutions, which are orange colored, e.g., $\{x_1, x_4, x_1\}$, $\{x_1, x_4, x_5\}$, $\cdots$, $\{x_3, x_4, x_6\}$ for Ψ_1, $\{x_1, \bar{x}_2, x_1\}$, $\{x_1, \bar{x}_2, x_5\}$, $\cdots$, $\{x_3, \bar{x}_2, x_6\}$ for Ψ_2, and $\{x_1, \bar{x}_2, x_1\}$, $\{x_1, \bar{x}_2, \bar{x}_3\}$, $\cdots$, $\{x_3, \bar{x}_2, x_6\}$ for Ψ_3.

For comparison, the insets of Figs. 2(d)–2(f) show a numerical simulation of the same physical process traced with a Lindbladian equation taking into account experimental error sources such as the spontaneous decay rate ($\gamma/2\pi = 30$ kHz) and laser phase noise. The numerical simulations are conducted to compare our experimental results of the experimental graphs G_1^{Exp}, G_2^{Exp}, and G_3^{Exp}. We take into account the spontaneous decay from the intermediate state $|i\rangle$, in calculating the Lindblad equation given by

$$\frac{d\rho}{dt} = -\frac{i}{\hbar}[H, \rho] + \sum_{j=1}^{N}\left(L_j \rho L_j^{\dagger} - \frac{1}{2}\{L_j^{\dagger} L_j, \rho\}\right), \quad (5)$$

where ρ is the density matrix, H is the system Hamiltonian, and $L_j = \sqrt{\gamma_i/2}\sigma_z^{(j)}$ is the Lindblad operator. For our detuning from $|i\rangle$ and the Rabi frequencies, the scattering rate to $|i\rangle$ is estimated to be $\gamma = (2\pi)\,30$ kHz. Then the numerical calculation is conducted with the Monte Carlo method to consider the laser phase noise, according to a measured spectral density of the noise which is about 10^4 rad^2/Hz in the range of the MHz. We also consider the nonuniform Rabi frequencies of the individual atoms, which are 85%–99.8% from the Rabi frequency at the laser beam center, due to the finite diameter of 50 μm and the fluctuation of atom positions $\delta x = 0.1$ μm, $\delta y = 0.1$ μm, $\delta z = 0.6$ μm [17]. The difference between the simulation and experiment is attributed to mainly the distance error between atoms and the laser beam center, which results in nonuniform Rabi frequencies of atoms in Eq. (3).

Finally we determine whether the satisfiability of a 3-SAT instance is experimentally checkable, i.e., whether the total probability of the MIS solution states is measured higher than the corresponding random guess probability. In random guessing, we can substitute all possible $\{x_1, x_2, x_3, x_4, x_5, x_6\}$ cases to Ψ_1, Ψ_2, and Ψ_3. However, as x_4 is a do-not-care term in the Ψ_2 and Ψ_3 cases and similarly x_5 is a do-not-care term in the Ψ_3 case only, all $\{x_1, x_2, x_3, x_4, x_5, x_6\}$'s are applicable to Ψ_2, and Ψ_3 as well as Ψ_1. Numerical simulation finds that the random guessing probabilities are 53.13%, 53.13%, and 50% for Ψ_1, Ψ_2, and Ψ_3, respectively. In our experiments, the probabilities of the orange bars in Fig. 2(d) for G_1^{Exp} are summed to be 81%, significantly higher than the random guess probability 53.13% of this instance. Likewise, the satisfiabilities of Ψ_2 and Ψ_3 are sufficiently evaluable with the measured probabilities 78% (G_2^{Exp}) and 74% (G_3^{Exp}), higher than 53.13% and 50% of these instances, respectively.

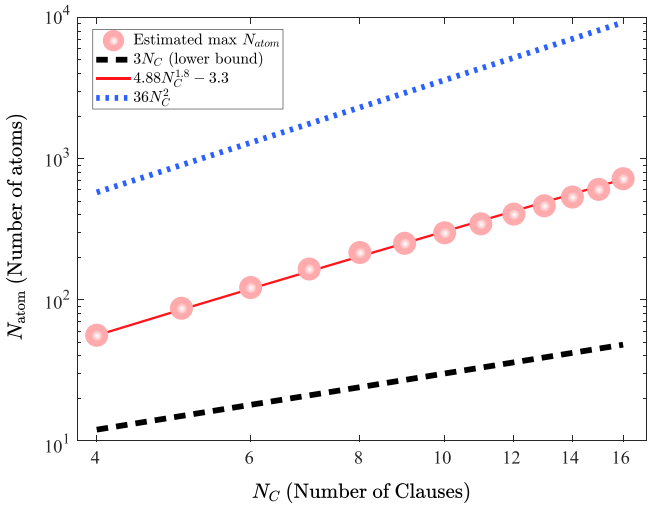

FIG. 4. Estimation of the required number of atoms for MIS graphs mapped from 3-SAT problems. The lower bound is estimated from 3-SAT instances with no negation literal pairs and restricted to $3N_C$ (black dashed line). The upper bound is calculated from 3-SAT instances with maximal negation literal pairs (red dots) and scaled to $4.88{N_C}^{1.8}$ (solid line). It is also compared with the scaling result when the "crossing lattice" scheme is used (blue dotted line).

VI. DISCUSSION

While all MIS graphs are in principle implementable in the three-dimensional space with quantum wires [17], it is worthwhile to discuss the scaling issue of the Rydberg atom approach to the 3-SAT problem. First, we estimate the number of atoms, N_A, necessary for general 3-SAT instances. For a Boolean expression that has N_C clauses, the lower bound is $N_A \gtrsim 3N_C$. The upper bound is the case of maximal literal-negation pairs, as the corresponding MIS graph has maximal interclause interactions. Physical implementation requires auxiliary atoms using either the "crossing lattice" scheme [31] or the "quantum wire" scheme [17], both of which have recently been suggested and are experimentally demonstrable. In the "crossing lattice" scheme, each vertex is transformed to an atom chain on a 2D surface, and the interactions between the vertices are implemented with "crossing gadgets" of at most 8 atoms. So, the upper bound of N_A is estimated to be $36{N_C}^2$ for a $3N_C$-vertex nonunit disk graph with arbitrary connectivity. In the "quantum wire" scheme, we numerically estimate the upper bound of the required number of atoms for implementing the MIS graphs as in Fig. 4, where we assume all interclause interactions are implemented with quantum wires consisting of an average of 4 atoms. The upper bound of the total number of atoms scales as $\sim 4.88{N_C}^{1.8}$, obtained from the curve fit of calculated values (solid line), being compared with the scaling of the "crossing lattice" scheme (blue dotted line). So, in the "quantum wire" scheme,

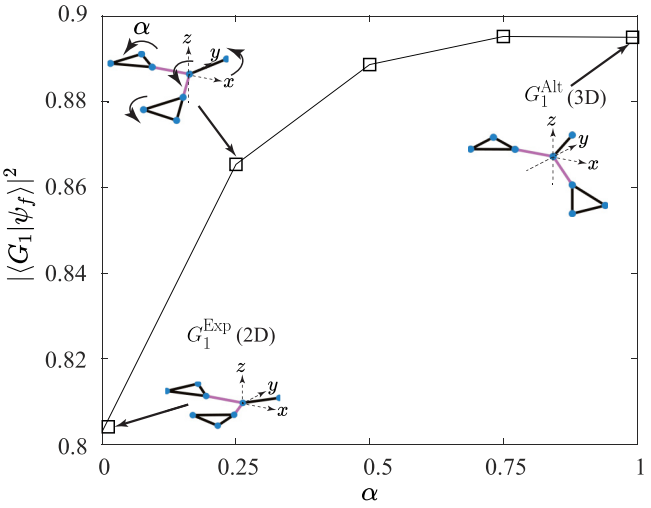

FIG. 5. Ground-state fidelity $|\langle G_1|\psi_f\rangle|^2$ according to the structural deformation from $G_1^{\rm Exp}$ to $G_1^{\rm Alt}$ with respect to a normalized rotation angle α.

the required number of total atoms is numerically estimated to be upper-bounded by a scaling of ${N_C}^{1.8}$ for the case of maximal literal-negation pairs and linear to N_C for the case of maximum degree 6 in 3D [32].

We can estimate the experimental time budget to access a large-scale 3-SAT problem. The probability to successfully obtain the solutions of the 3-SAT problem, after M experimental repetitions, is given by

$$P_s(p,M)=\sum_{j=1}^{M}(1-p)^{j-1}p=1-(1-p)^M, \qquad (6)$$

where p is the ground-state probability of the corresponding MIS graph of N_A atoms. With the experimental scaling $p\sim 1.04^{-N_A}$ of a state-of-the-art experimental platform [18], the ground-state probability of an $N_A=400$ MIS graph is estimated to be $p(N_A=400)\sim 10^{-7}$. The required number of repetitions to achieve $P_s>20\%$, for example, is given by $M>\log_{10}0.8/\log_{10}(1-p)$, which estimates about $M\sim 10^6$ experimental repetitions. So, an $N_A=400$ MIS graph experiment, which can serve 3-SAT instances with approximately $12\sim 140$ clauses, would take one week in the typical repetition rate of $2\sim 3$ Hz of the current experimental platforms.

Technical improvements can be considered for future experiments, which include three-dimensional Rydberg atom graphs and adiabatic control path optimization. First, the fidelity of the many-body ground state depends on the residual interactions between the atoms placed outside the blockade distance d_B, which are small but not zero. So arranging atoms in the full three-dimensional space would be useful to describe the Hamiltonian $\hat{H}(G)$ as exactly as possible so that the long-range interactions are minimized. In Fig. 5, we calculate the fidelity $|\langle H(G_1^{\rm Exp})|\Psi_f\rangle|^2$, where $|H(G_1^{\rm Exp})\rangle$ is the analytic many-body ground state of $H(G_1^{\rm Exp})$ and $|\Psi_f\rangle$ is the numerically estimated final many-body state after the quasiadiabatic evolution under our experimental condition (without decoherence taken into account). For the experimental graph $G_1^{\rm Exp}$ in 2D, the fidelity is estimated to be 81%, due to the contribution of long-range residual Rydberg interactions among atoms spaced beyond the Rydberg blockade radius. In our atomic arrangements for $G_1^{\rm Exp}$, the average strength of the residual interactions is $\langle U_{\rm res}\rangle/2\pi=0.64$ MHz, and their distribution is asymmetric. However, we can transform the structure of $G_1^{\rm Exp}$ to an alternative graph $G_1^{\rm Alt}$, which is more symmetric in geometry (see Table II for atomic positions). A structural transformation is conducted as in Fig. 5, by rotating the clauses C_0, C_1, and C_2 with respect to the edges from the literal atom $\bar{x}_1$ (central atom), respectively. These geometric changes are parametrized to a normalized rotation angle α (0 at $G_1^{\rm Exp}$, and 1 at $G_1^{\rm Alt}$). For the graph $G_1^{\rm Alt}$, the average residual interaction strength is reduced to $\langle U_{\rm res}\rangle/2\pi=0.40$ MHz. Then it is found that the ground-state fidelity $|\langle H(G_1^{\rm Exp})|\Psi_f\rangle|^2$ after the same quasiadiabatic evolution is improved to 90%. So three-dimensional atom allocations have more degrees of freedom for better experimental performances. Figure 5 shows the improvement of the ground-state fidelity $|\langle G_1|\psi_f\rangle|^2$ during the structural transformation. We expect to compare the experimental fidelity of the suggested 3D atomic graph $G_1^{\rm Alt}$ in the near future, though we cannot currently make the experimental consistency between 2D and 3D graphs. The existing experimental errors such as the hardness of preparing the uniform 3D traps and imaging them are to be overcome.

Adiabatic control path optimization can be also considered. For example, along the Hamiltonian path in Fig. 3, the optimal time schedule of the annealing path $\Delta(t)$ during the constant $\Omega(t)$ might be other than the linear ramps due to the structure of the eigenenergy landscape in the control path. One way to find a time schedule for obtaining better ground-state probability is to apply an adiabaticity parameter $\gamma=|\delta E^2(t)/\dot{\Delta}(t))|$, where $\delta E(t)$ is the energy gap between the ground and the first excited eigenstates at t. Then the proper time schedule of $\Delta(t)$ can be found within a regime of $\gamma\gg 1$ for all t [33]. For larger and more complex problem instances in which the energy gaps are hard to be known, closed-loop optimization methods might be applied. An ansatz of the control path is initially guessed, then updated according to the overlap of the ground state of the system. The recently suggested approaches of closed-loop optimizations are using genetic [34] and variational [35] methods. In the genetic approach, the time schedule $\Delta(t)$ is often modeled to a polynomial ansatz, then the coefficients of the polynomial are found to optimize the ground-state probability after the adiabatic evolution. In the variational approach, the entire time window for adiabatic evolution is divided into several chunks. For L chunks, the detunings Δ_i in each chunk where $i\in\{1,\cdots,L\}$ are to be found. The annealing path becomes the piecewise linear sweeps between adjacent detunings Δ_i.

VII. CONCLUSION

In summary, Rydberg atom interactions have been used to encode and solve the 3-SAT problem, a task involving determining the satisfiability of a Boolean function. The proposed Rydberg 3-SAT algorithm achieves this by constructing a general Boolean function using the three types of building blocks: Rydberg atom dimers, trimers, and quantum wires. The satisfiability of the function is then ascertained by searching

for its ground state within the structured Rydberg atom arrangement. Consequently, this implementation of the 3-SAT problem through a Rydberg atom graph has the potential to encode various decision-based computational challenges associated with NP problems. It is noted that the presented proof-of-principle experiments do not imply computational advantage over classical heuristic solvers. Instead, their value lies in surpassing classical brute force methods. To advance the Rydberg atom approach toward quantum computing further, not only technical improvements of Rydberg atom experiments but also quantum-classical combined algorithmic developments are warranted.

ACKNOWLEDGMENT

This research is supported by Samsung Science and Technology Foundation (Grant No. SSTF-BA1301-52).

[1] F. Arute, K. Arya, R. Babbush *et al.*, Quantum supremacy using a programmable superconducting processor, Nature (London) **574**, 505 (2019).

[2] C. Monroe, W. C. Campbell, L.-M. Duan *et al.*, Programmable quantum simulations of spin systems with trapped ions, Rev. Mod. Phys. **93**, 025001 (2021).

[3] S. Ebadi, T. T. Wang, H. Levine *et al.*, Quantum phases of matter on a 256-atom programmable quantum simulator, Nature (London) **595**, 227 (2021).

[4] P. Shor, Algorithms for quantum computation: Discrete logarithms and factoring, in *Proceedings of the 35th Annual Symposium on Foundations of Computer Science* (IEEE, New York, 1994), pp. 124–134.

[5] L. K. Grover, Quantum mechanics helps in searching for a needle in a Haystack, Phys. Rev. Lett. **79**, 325 (1997).

[6] S. A. Cook, The complexity of theorem proving procedures, in *Proceedings of the Third Annual ACM Symposium on Theory of Computing* (ACM, New York, 1971).

[7] E. Farhi, J. Goldstone, S. Gutmann, J. Lapan, A. Lundgren, and D. Preda, A quantum adiabatic evolution algorithm applied to random instances of an NP-complete problem, Science **292**, 472 (2001).

[8] N. G. Dickson and M. H. S. Amin, Does adiabatic quantum optimization fail for NP-complete problems? Phys. Rev. Lett. **106**, 050502 (2011).

[9] F. Barahona, On the computational complexity of Ising spin glass models, J. Phys. A: Math. Gen. **15**, 3241 (1982).

[10] S. Arora and B. Barak, *Computational Complexity: A Modern Approach* (Cambridge University Press, Cambridge, 2009).

[11] J. Zhu, A. Salhotra, C. R. Meinecke, P. Surendiran, R. Lyttleton, D. Reuter, H. Kugler, S. Diez, A. Månsson, H. Linke, and T. Korten, Solving the 3-SAT problem using network-based biocomputation, arXiv:2203.17154.

[12] R. Zhang, J. Chen, and H. Zhao, Procedure of solving 3-SAT problem by combining quantum search algorithm and DPLL algorithm, Perform. Commun. Syst. **4**, 14 (2020).

[13] Y. Zhang, Y-x. Bian, Q. Fan, and J. Chen, Quantum solution for the 3-SAT problem based on IBM Q, in *Cloud Computing, Smart Grid and Innovative Frontiers in Telecommunications*, edited by X. Zhang *et al.* (Springer, New York, 2020), pp. 410–423.

[14] A. Lucas, Ising formulations of many NP problems, Front. Phys. **2**, 5 (2014).

[15] V. Choi, Adiabatic quantum algorithms for the NP-complete maximum-weight independent set, exact cover and 3SAT problems, arXiv:1004.2226.

[16] H. Pichler, S.-T. Wang, L. Zhou, S. Choi, and M. D. Lukin, Quantum optimization for maximum independent set using Rydberg atom arrays, arXiv:1808.10816.

[17] M. Kim, K. Kim, J. Hwang, E.-G. Moon, and J. Ahn, Rydberg quantum wires for maximum independent set problems, Nat. Phys. **18**, 755 (2022).

[18] S. Ebadi *et al.*, Quantum optimization of maximum independent set using Rydberg atom arrays, Science **376**, 1209 (2022).

[19] H. K. Büning and T. Lettmann, *Propositional Logic: Deduction and Algorithms* (Cambridge University Press, Cambridge, 1999).

[20] R. M. Karp, Reducibility among combinatorial problems, in *Complexity of Computer Computations*, edited by R. E. Miller *et al.* (Plenum Press, New York, 1972).

[21] M. R. Garey and D. S. Johnson, *Computers and Intractability: A Guide to the Theory of NP-Completeness* (W. H. Freeman, New York, 1979).

[22] Y. Song, M. Kim, H. Hwang, W. Lee, and J. Ahn, Quantum simulation of Cayley-tree Ising Hamiltonians with three-dimensional Rydberg atoms, Phys. Rev. Res. **3**, 013286 (2021).

[23] A. Byun, M. Kim, and J. Ahn, Finding the maximum independent sets of Platonic graphs using Rydberg atoms, PRX Quantum **3**, 030305 (2022).

[24] X. Qiu, P. Zoller, and X. Li, Programmable quantum annealing architectures with Ising quantum wires, PRX Quantum **1**, 020311 (2020).

[25] S. Weber *et al.*, Hardware considerations for high-connectivity quantum annealers, APS March Meeting Abstracts No. A33-008 (Bulletin of the American Physical Society, 2018).

[26] W. Lee, M. Kim, H. Jo, Y. Song, and J. Ahn, Coherent and dissipative dynamics of entangled few-body systems of Rydberg atoms, Phys. Rev. A **99**, 043404 (2019).

[27] S. Fey, S. C. Kapfer, and K. P. Schmidt, Quantum criticality of two-dimensional quantum magnets with long-range interactions, Phys. Rev. Lett. **122**, 017203 (2019).

[28] P. Scholl, M. Schuler, H. J. Williams *et al.*, Quantum simulation of 2D antiferromagnets with hundreds of Rydberg atoms, Nature (London) **595**, 233 (2021).

[29] Y. S. Teo, H. Zhu, B. G. Englert, J. Rehacek, and Z. Hradil, Quantum-state reconstruction by maximizing likelihood and entropy, Phys. Rev. Lett. **107**, 020404 (2011).

[30] S. de Léséleuc, D. Barredo, V. Lienhard, A. Browaeys, and T. Lahaye, Analysis of imperfections in the coherent optical excitation of single atoms to Rydberg states, Phys. Rev. A **97**, 053803 (2018).

[31] M.-T. Nguyen, J.-G. Liu, J. Wurtz, M. D. Lukin, S.-T. Wang, and H. Pichler, Quantum optimization with arbitrary connectivity using Rydberg atom arrays, PRX Quantum **4**, 010316 (2023).

[32] C. Dalyac and L. Henriet, Embedding the MIS problem for nonlocal graphs with bounded degree using 3D arrays of atoms, arXiv:2209.05164.

[33] P. Richerme, C. Senko, J. Smith, A. Lee, S. Korenblit, and C. Monroe, Experimental performance of a quantum simulator: Optimizing adiabatic evolution and identifying many-body ground states, Phys. Rev. A **88**, 012334 (2013).

[34] P. R. Hegde, G. Passarelli, A. Scocco, and P. Lucignano, Genetic optimization of quantum annealing, Phys. Rev. A **105**, 012612 (2022).

[35] B. F. Schiffer, J. Tura, and J. I. Cirac, Adiabatic spectroscopy and a variational quantum adiabatic algorithm, PRX Quantum **3**, 020347 (2022).